Band structure engineering and efficient charge transport in oxygen substituted g-C$_3$N$_4$ for superior photocatalytic hydrogen evolution

Chengyin Liu[a], Hongwei Huang[a,*], Wen Cui[b], Fan Dong[b], Yihe Zhang[a,*]

[a] Beijing Key Laboratory of Materials Utilization of Nonmetallic Minerals and Solid Wastes, School of Materials Science and Technology, China University of Geosciences, Beijing 100083, PR China
[b] College of Environmental and Biological Engineering, Chongqing Technology and Business University, Chongqing 400067, PR China

ARTICLE INFO

ABSTRACT

Graphitic carbon nitride (g-C$_3$N$_4$) is one of the cardinal semiconductor photocatalysts to address the energy crisis issues. Howbeit, it remains a large challenge to explore effective strategies to confront its flaws, such as insufficient response to solar spectrum and less efficient charge separation. Here, we report development of a wide-range-photoresponsive O substituted g-C$_3$N$_4$ with tunable band structure and efficient charge separation by an one-pot co-pyrolysis of melamine and substantial ammonium acetate, and the O substitution concentration can be largely adjusted from 0.68% to 5.59% by controlling the ammonium acetate amount. Experimental and theoretical results uncovered that the O atoms were incorporated into the g-C$_3$N$_4$ lattice by replacing the C−N═C coordinated N atoms to form C−O═C bonds. This atomic substitution introduces an acceptor level below conduction band of g-C$_3$N$_4$, which not only broadens visible-light response of g-C$_3$N$_4$ to 800 nm with adjustable band gap, but also greatly promotes the carrier density, bulk charge separation and surface charge transfer efficiency. Thus, this advanced O substituted g-C$_3$N$_4$ casts significantly enhanced photocatalytic hydrogen evolution activity, achieving ∼9-fold enhancement compared to bulk g-C$_3$N$_4$ under visible light irradiation with a high apparent quantum efficiency (AQE) of 13.2% at 420 nm, exceeding most of the reported doped g-C$_3$N$_4$. Besides, this synthetic route is also applicable to preparation of O substituted g-C$_3$N$_4$ with other precursors, such as urea and thiourea, highlighting the universality of the current strategy. The study offers a new perspective into exploitation of high-performance catalysts for solar energy conversion with a facile and general decoration strategy.

1. Introduction

Semiconductor photocatalysis has gained extensive attention owing to their potential applications in solar-energy-driven hydrogen evolution, which is one of the most efficient approaches for developing clean and sustainable energy [1–7]. Metal-free graphitic carbon nitride (g-C$_3$N$_4$), a charming polymeric organic semiconductor, has attracted great interest due to its high thermal and chemical stability, charming electronic structure and low cost [8,9]. Regrettably, g-C$_3$N$_4$ is responsive insufficiently to solar spectrum, and particularly the high recombination rate of photo-generated electron-hole pairs also suppresses the improvement of photocatalytic activity [10–12]. Therefore, developing an appropriate way to broaden the visible-light-response and promote the charge separation efficiency is necessary for further development of g-C$_3$N$_4$. Up to now, the widely adopted protocols for improving the photocatalytic activity of g-C$_3$N$_4$ involve microstructure modification [13–16], heterojunction fabrication [17–20], noble metal

deposition [21–23], and elemental doping [24–32]. Among these various strategies, the doping of framework with a heteroatom, especially non-metal elements (such as N, C, F, P, O and S) [24–32], has been widely researched because of its effectiveness in ameliorating the electronic structures for water splitting reaction.

Recently, She et al. [30] obtained oxygen-modified g-C$_3$N$_4$ materials with high crystallinity by calcinating melamine for three times. The oxygen modified sample with 2D monolayer structure possesses large surface area, enhanced bandgap and efficient electrons/holes separation, jointly benefiting the photocatalytic activity. Huang et al. [31] synthesized O-doped g-C$_3$N$_4$ with porous network by a precursor pretreatment method. The porous network and appropriate O doping not only enhance the light harvesting but also promote charge separation through forming an internal electric field. Wang et al. [32] reported a hollow microsphere O doped g-C$_3$N$_4$catalyst with improved visible light absorption and charge separation efficiency through using an acetonitrile-assisted solvothermal method at low temperature. The above work

demonstrated that O doped g-C$_3$N$_4$ photocatalysts can be obtained via different synthetic approaches, and they all display improved photocatalytic performance. In particularly, the enhanced photocatalytic activities in these O doped g-C$_3$N$_4$ stem from distinct mechanisms. This charming phenomenon attracts our attention to explore new photocatalytic mechanism for O doped g-C$_3$N$_4$ which is achieved by other synthetic strategies.

Our group found that the ammonium salts can play different roles in the synthesis of high-performance g-C$_3$N$_4$ materials by facile co-pyrolysis with melamine. Ammonium bicarbonate (NH$_4$HCO$_3$) and melamine produce porous g-C$_3$N$_4$ with up-shifted conduction band (CB) position, rendering highly promoted separation and transfer efficiency of charge carriers for highly improved photocatalytic performance toward RhB degradation, NO removal, and hydrogen evolution [33]. Ammonium chloride (NH$_4$Cl) and melamine generate chlorine (Cl) intercalated g-C$_3$N$_4$, which endows g-C$_3$N$_4$ with remarkably promoted charge migration efficiency by introducing the advantages of establishing interlayer charge transfer pathway, porous structure, narrowed band gap, up-shifted conduction-band (CB) level as well as enhanced surface area, resulting in excellent photocatalytic performance for H$_2$ evolution, CO$_2$ reduction, liquid and air pollutants removal [34]. Co-pyrolysis of ammonium bromide (NH$_4$Br) and melamine yields a horn-like hollow mesoporous ultrathin g-C$_3$N$_4$ tube via first giving birth to a horn-like Br-containing intermediate and then furthering decomposition transformation. This special structure (hollow/mesoporous/ultrathin/horn-like) allows g-C$_3$N$_4$ outstanding photocatalytic performance for hydrogen evolution and CO$_2$ reduction [13]. These interesting phenomena drive us to explore the different effects of other ammonium salts on the synthetic process of advanced g-C$_3$N$_4$ materials.

In this work, we successfully obtained an oxygen substituted g-C$_3$N$_4$ photocatalyst by introduction of substantial ammonium acetate in the thermal polymerization process of melamine and disclosed a new mechanism of photo-induced charge carriers separation. To our best knowledge, it is the first time to report this facile approach to synthesis of O doped g-C$_3$N$_4$ by using melamine and ammonium acetate as co-precursors, and similar results can also be obtained using other nitrogen-rich precursors (such as urea and thiourea) for replacing melamine, highlighting the universality of the current strategy. Based on systematical characterizations and density functional theory (DFT) calculations, it is demonstrated that the O atoms replace lattice N atoms to form the C−O═C bonds, which drastically broadens the visible-light response of g-C$_3$N$_4$ from 450 nm to 800 nm and gives rise to largely narrowed band gap of g-C$_3$N$_4$, and these properties can be continuously adjusted by controlling the O doping concentration. In particular, the O substitution for the first time introduces an acceptor level below CB, which greatly promotes carrier density, bulk charge separation and surface charge transfer efficiency. Thus, the O substituted g-C$_3$N$_4$ here exhibits prominently enhanced visible-light-driven hydrogen evolution activity with a high apparent quantum efficiency (AQE) of 13.2% at 420 nm, exceeding most of the reported doped g-C$_3$N$_4$. The current study presents a simple and effective way for synergistically optimizing the electronic structure, optical response and photocatalytic properties for g-C$_3$N$_4$-based materials.

2. Experimental details

2.1. Synthesis

The two raw materials of ammonium acetate (Sinopharm Chemical Reagent Co., Ltd, 98%) and melamine (Sinopharm Chemical Reagent Co., Ltd, 99%) were of analytic grade and without other purification. The simple preparation method is as follows: melamine (1 g) and a certain amount of ammonium acetate were uniformly mixed and ground thoroughly. Then the powders were put into muffle furnace and heated at 520 °C for 2 h with a heating rate of 1.7 °C/min. When the program is finished, the furnace was cooled to room temperature

Table 1
Results of organic elemental analyses for g-C$_3$N$_4$ and O-CNX (X = 1–3).

Sample	melamine/ CH$_3$COONH$_4$ molar ratio	C/N	%			
			N	C	H	O
g-C$_3$N$_4$	0	0.556	62.73	34.89	1.70	0.68
O-CN1	1/5	0.564	61.97	34.98	2.01	1.04
O-CN2	1/10	0.569	61.27	34.84	1.86	2.03
O-CN3	1/30	0.570	59.03	33.66	1.72	5.59

automatically. The samples with molar ratios of ammonium acetate to melamine of 5, 10, and 30 were signed as O-CN1, O-CN2, and O-CN3, respectively. Samples prepared in the same way using urea and thiourea as precursors for replacing melamine were denoted as O-UCN and O-TCN, respectively. The molar ratios of ammonium acetate to urea and thiourea are 0.5 and 1, respectively. Bulk carbon nitride products prepared by melamine, urea and thiourea without adding ammonium acetate were labeled as g-C$_3$N$_4$, UCN and TCN, respectively. Following the synthesis, all products were collected and washed repeatedly with deionized water, and then dried at 60 °C for 10 h.

2.2. Characterization

The chemical states were analyzed by X-ray photoelectron spectroscopy (XPS), with 150 W Al Kα X-ray irradiation (Thermo ESCALAB 250, USA). Thermogravimetric (TG) analysis was performed on a Labsys TGDTA16 (SETARAM) thermal analyzer. Scanning electron microscopy (SEM) measurements were carried out with a HITACHI S-4800 microscope, and the microstructures were tested by transmission electron microscopy (TEM) (JEM-2100 JEOL, Japan). UV–vis diffuse reflectance spectra (DRS) of the samples were recorded by UV–vis spectrophotometer (Varian Cary 5000). The phase structures of g-C$_3$N$_4$, O-CN1, O-CN2, and O-CN3 were examined by X-ray diffraction (XRD) on Bruker with Cu Kα radiation. The Fourier-transform infrared (FTIR) spectra were recorded by a Bruker spectrometer in the frequency range of 4000 cm^{-1}–450 cm^{-1}. The specific surface areas of samples were measured by the nitrogen adsorption BET method (USA, Micromeritics ASAP 2460). The surface photovoltage (SPV) tests were conducted on a home-built apparatus, including a lock-in amplifier (SR830) and a light chopper (SR540). The photoluminescence (PL) spectra were measured by a Hitachi F-4600 fluorescence spectrophotometer at room temperature. Organic elemental analysis (OEA) was measured by Elementar Analysensysteme GmbH vario EL instrument.

2.3. Photocatalytic H$_2$ evolution

The photocatalytic activity was evaluated by the hydrogen production using a closed-cycle gas circulation system with Pyrex glass. The generated gas was detected using a Labsolar-III (AG) gas chromatograph furnished with high purity argon as carrier gas, which was a whole system. In the experiment, the Pt as cocatalyst was loaded on the photocatalysts using the ultraviolet radiation reduction treatment from H$_2$PtCl$_6$ aqueous solution. Then, the 50 mg photocatalyst with Pt (1% wt) was dispersed in 100 ml solution containing 90 ml deionized water and 10 ml lactic acid. The incident light was provided by a 300 W Xe lamp with 420 nm filter at room temperature.

An apparent quantum efficiency (AQE) for H$_2$ evolution was measured using the same experimental setup, but with 80 mg of catalyst and a 300 W Xe lamp equipped with a series of band-pass filters. The light densities of incident light were 5.4, 5.8, 6.3, 6.6, 6.4 mW cm^{-2} for the 420, 450, 500, 550 and 600 nm filters, respectively (PLS-MV2000 photoradiometer). The irradiated surface area was about 33 cm^2. The peak width of all the band-pass filters is 15 nm. The AQE was calculated by the following equation:
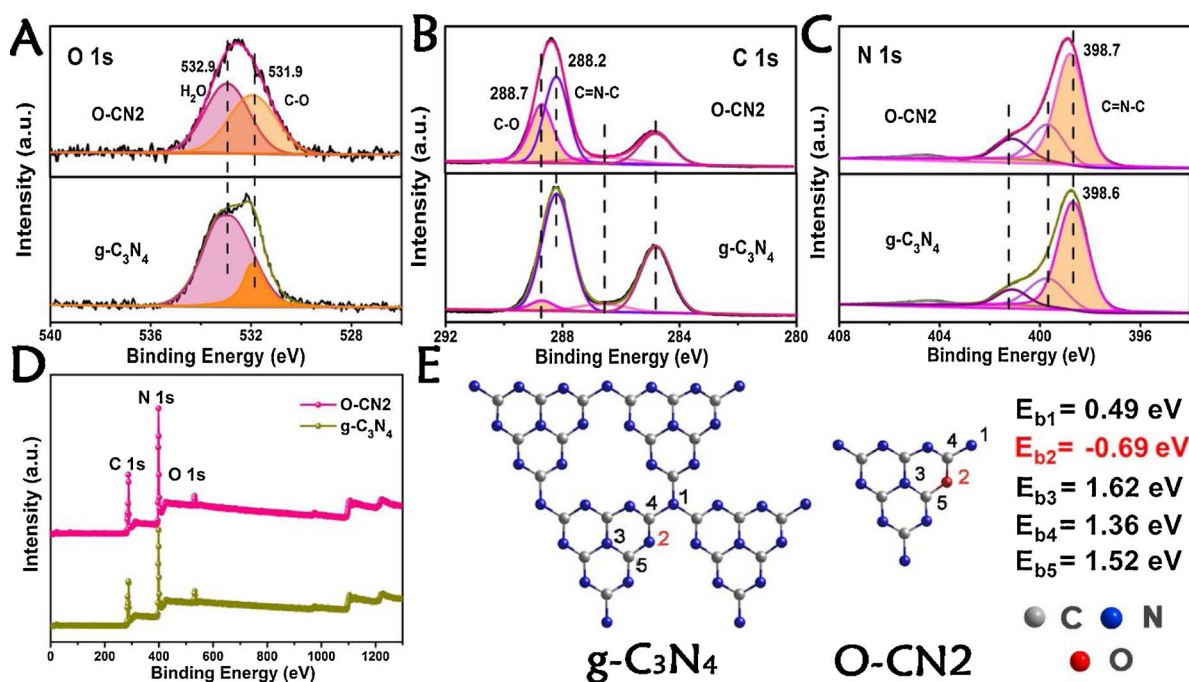
Fig. 1. (A) O 1s, (B) C 1s and (C) N 1s high resolution XPS spectra of the bulk g-C$_3$N$_4$ and O-CN2. (D) XPS survey spectra of g-C$_3$N$_4$ and O-CN2. (E) Optimized structures of g-C$_3$N$_4$ and O-CN2. E$_b$ stands for doping energy, negative means heat release.

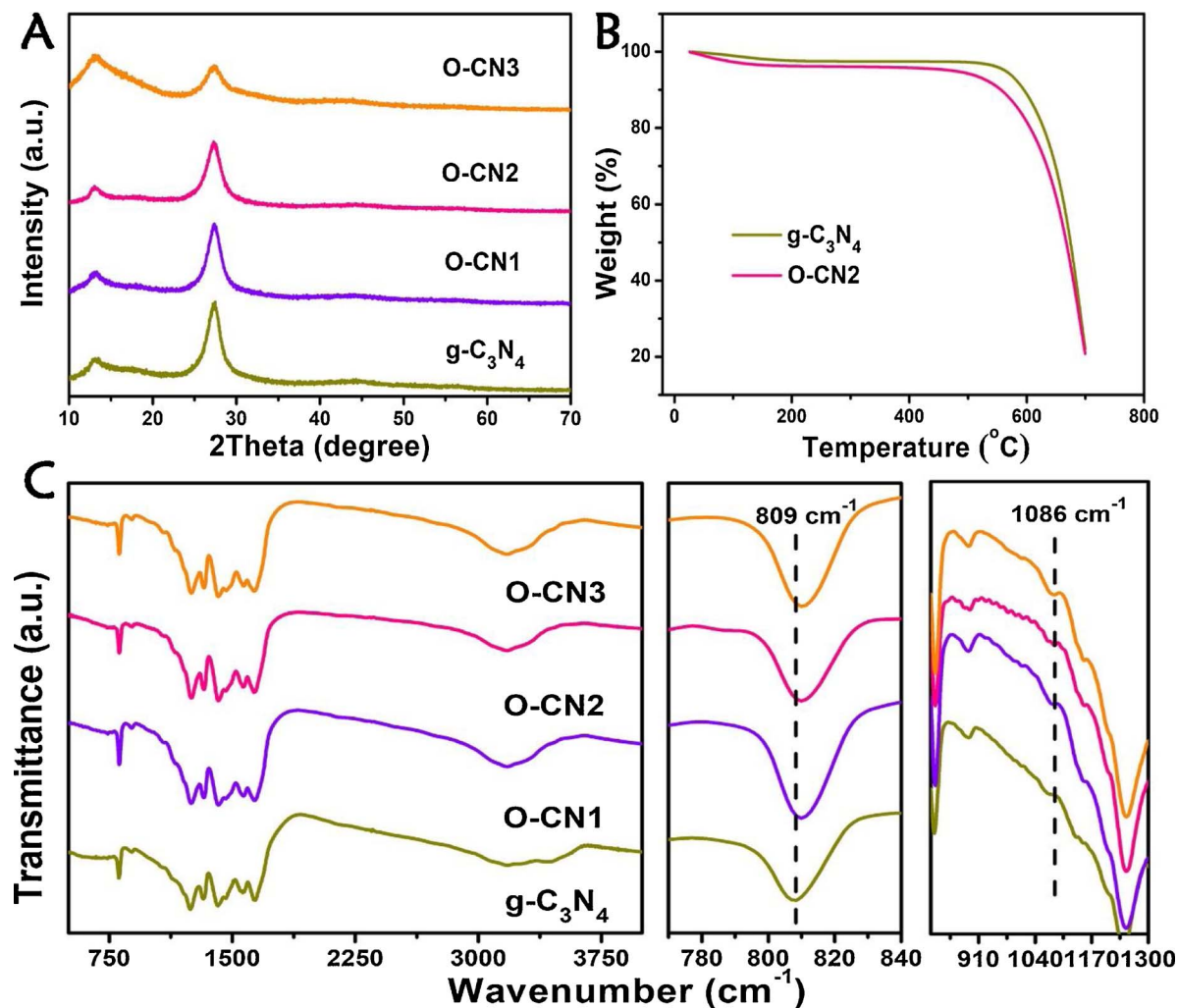**Fig. 2.** (A) XRD patterns of g-C$_3$N$_4$ and O-CNX (X = 1–3) samples. (B) TG curves of g-C$_3$N$_4$ and O-CN2. (C) FTIR spectra of g-C$_3$N$_4$ and O-CNX (X = 1–3) samples.
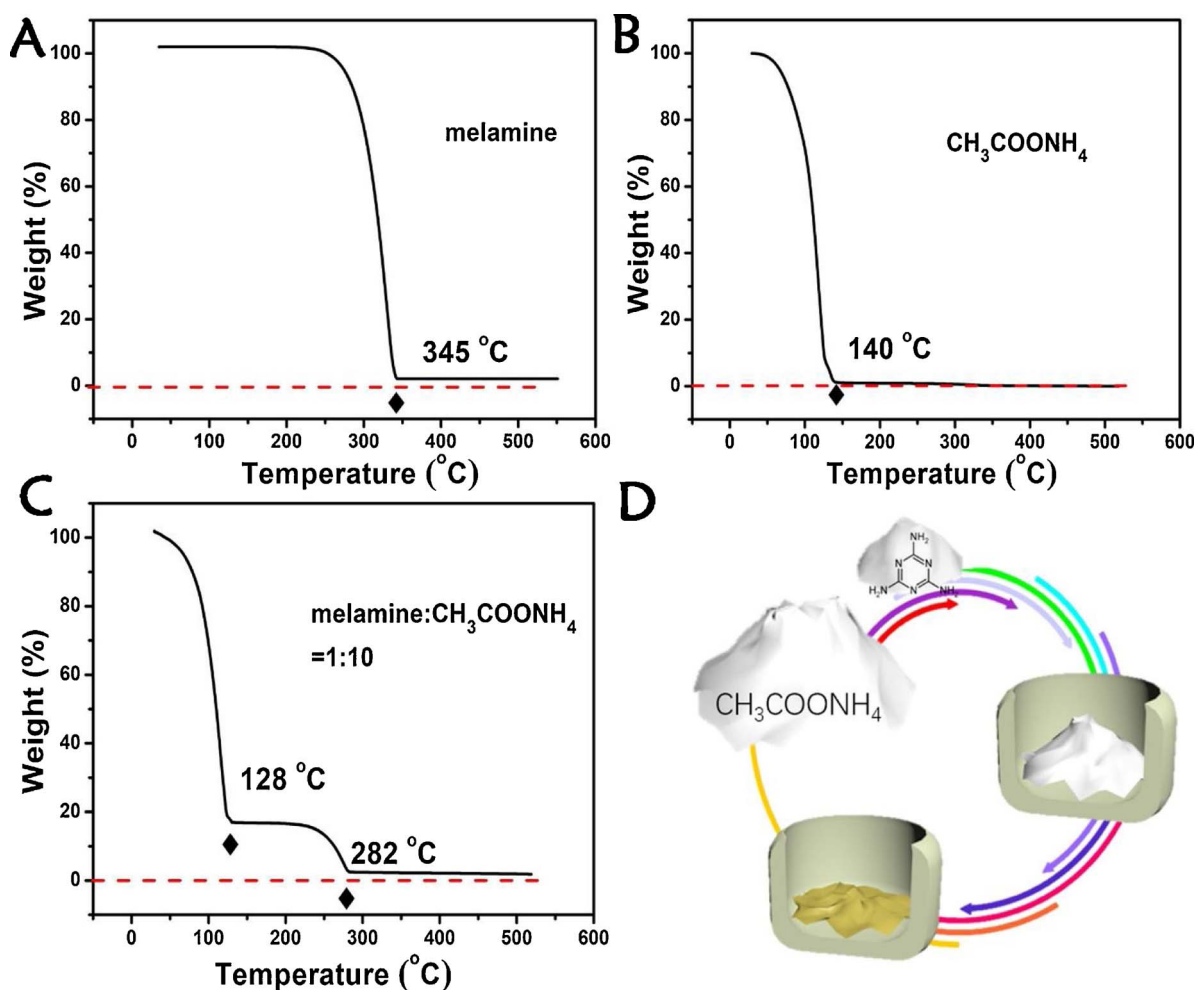
Fig. 3. TG curve of (A) melamine, (B) NH_3COONH_4 and (C) melamine/NH_4Br mixture = 1/10. (D) Schematic illustration of preparation for O doped g-C_3N_4.

AQY (%) = umber of evolved H_2 molecules × 2 × 100/number of incident photons

2.4. Photoelectrochemical measurements

Photoelectrochemical measurements were performed with an electrochemical workstation in a 0.1 mol L^{-1} Na_2SO_4 aqueous electrolyte. Saturated calomel electrode (SCE) and platinum filament were used as reference and counter electrode, respectively. 10 mg of catalyst powder was dispersed in 0.5 ml of solution containing 480 μL of deionized water and 20 μL of Nafion solution, and the mixed solution was under ultrasound for 30 min. Then the above solution was dropped onto the IFO film and dried at 80 °C for 10 h. The transient photocurrent was obtained by using a 30 s on-o−ff light cycle at a bias voltage of 0 V. Methylviologen dichloride ($MVCl_2$) was added into the electrolyte (0.1 M Na_2SO_4) to survey the surface charge transfer efficiency and charge carriers density. Electrochemical impedance spectra were collected in the frequency range from 1–10^5 Hz with a 5 mV sinusoidal AC voltage. The Mott-Schottky plots were measured at the frequency of 100 Hz. The visible light source came from a 300 W Xe lamp with a filter (λ > 420 nm).

2.5. DFT Calculations

Spin-polarized DFT-D2 calculations [35] were conducted using the "Vienna ab initio simulation package" (VASP5.4) [36,37] applying a generalized gradient correlation functional. [38] A plane-wave basis set

with cut-off energy 450 eV within the framework of the projector-augmented wave method was employed [39,40]. The Gaussian smearing width was set as 0.2 eV. The Brillouin zone was a 3 × 3 × 1 Monkhorst Pack grid. All atoms were converged to 0.01 eV $Å^{-1}$. A 3 × 3 × 1 supercell of monolayer g-C_3N_4 was first relaxed, the calculated N−C bond length is consistent with the published values [41].

The doping energy (E_b) is defined as:

$$E_b = E_{O\ doped\ g-C_3N_4} - \left(E_{g-C_3N_4} + E_O\right)$$

where E_O refers to the total energy of O species, which is calculated from the isolated O_2 molecules.

3. Results and discussions

Organic elemental analysis (OEA) was first performed to survey the effects of CH_3COONH_4 treatment on the bulk g-C_3N_4 and the composition change. As shown in Table 1, with the increase of CH_3COONH_4 amount in the co-precursors of melamine and CH_3COONH_4, the O content in as-prepared samples gradually increases from 0.68 to 5.59 corresponding to the samples from bulk g-C_3N_4 to O-CN3. Meanwhile, the N content decreased, and the C/N atomic ratio also shows an increase with the CH_3COONH_4 concentration. This result reveals that O atoms were doped into g-C_3N_4, which may replace N atoms.

The location of O atoms doping in g-C_3N_4 crystalline structure is investigated by X-ray photoelectron spectroscopy (XPS) spectra. As shown in Fig. 1A, the O1s high-resolution spectra can be deconvoluted into two peaks with the binding energy of 532.9 eV and 531.9 eV,
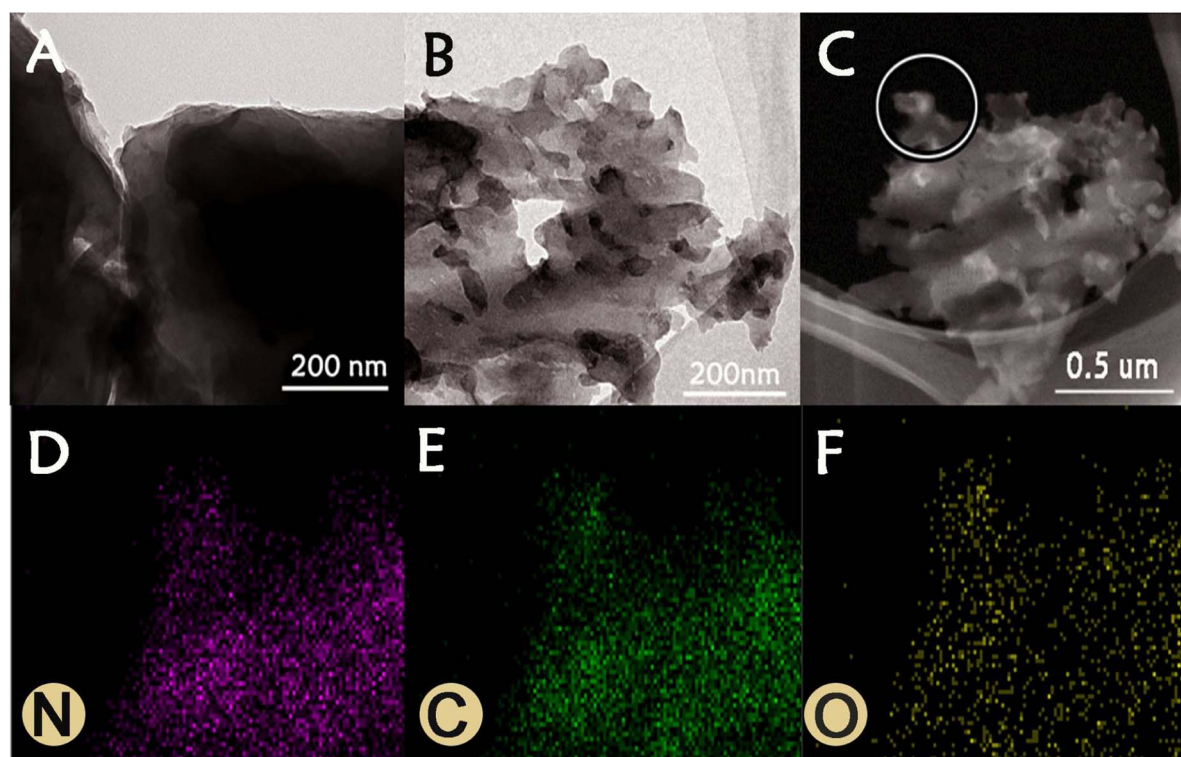
Fig. 4. TEM images of (A) g-C$_3$N$_4$ and (B) O doped g-C$_3$N$_4$ (O-CN2). EDX mapping (D) N atom, (E) C atom, and (F) O atom acquired from (C) O-CN2.

corresponding to surface adsorbed water and C−O (C═O), respectively. It is obvious that the intensity of C−O (C═O) bond of O−CN is higher than that of g-C$_3$N$_4$, demonstrating that more C−O (C═O) bonds appear in O−CN [31,32]. For the C1s high-resolution XPS spectra (Fig. 1B), the peak at 284.8 eV is due to the sp^2 C−C bonds, and those at 286.5 eV and 288.2 eV are ascribed to C−N bonds and sp^2 hybridized C (N−C═N), respectively. The highest binding energy of 288.7 eV can be attributed to the C−O (C═O) bonds [42–44], in which the intensity of O−CN is also stronger than that of g-C$_3$N$_4$, agreeing with the result of O1s high resolution spectra. The N1s (Fig. 1C) signals for g-C$_3$N$_4$ are fitted into three typical peaks with binding energies of 398.6, 399.6 and 401.2 eV, corresponding to C−N═C (sp^2 hybridized N), N−(C)$_3$groups and C−N−H bonds, respectively [45,46]. In particularly, the C−N═C bonds of O−CN sample at 398.7 eV display a small shift compared to that of g-C$_3$N$_4$, suggesting the alteration of C−N═C bonds. Besides, no signals ascribed to the N−O species are observed in the N 1s high resolution XPS spectrum [47] and no other elements can be detected in O−CN sample (Fig. 1D). The XPS results provide an evidence that O atoms were incorporated in the lattice of g-C$_3$N$_4$ by replacing the C−N═C coordinated N atoms.

In order to further confirm the location of O atoms in the g-C$_3$N$_4$ crystalline structure, density functional theory (DFT) calculation was employed. As shown in Fig. 1E, the corresponding doping energy (E$_b$) of substitutional O atom in the five possible doping positions of N (site1, 2 and 3) and C (site 4 and 5) is 0.49, −0.69, 1.62, 1.36 and 1.52 eV, respectively. Evidently, site 2 has the lowest doping energy among the five sites, which implies that site 2 is most likely to be the substitution site. The calculated result is well consistent with the above OEA and XPS conclusions and verifies that O atoms replace the lattice N atoms forming C−O═C bonds.

The XRD patterns were employed to investigate the crystal structures of g-C$_3$N$_4$ and O substituted g-C$_3$N$_4$ catalysts, as shown in Fig. 2A. The crystalline phase of O doped g-C$_3$N$_4$ is very similar to that of g-C$_3$N$_4$, confirming that the general structure of g-C$_3$N$_4$ is preserved by O substitution. The typical XRD peaks at 13.2° and 27.6° correspond to (100) in-planar peak and (002) interlayer-stacking peak, respectively

[48–50]. Compared with g-C$_3$N$_4$, it is obvious that O−CN shows the (002) peak with a low intensity, especially for O-CN3, which may indicate the thickness decrease of modified g-C$_3$N$_4$ samples [32]. It can be explained that CH$_3$COONH$_4$ reacts with melamine during the thermal-polymerization process, destroying the orderly stacking structure of g-C$_3$N$_4$ along [002] direction. According to the TG curves of g-C$_3$N$_4$ and O-CN2, it can be seen that the presence of O doping leads to a lower thermal stability (Fig. 2B) [51]. FTIR spectra of g-C$_3$N$_4$ and O−CN samples (Fig. 2C) display the typical molecular skeletal vibration modes in graphitic carbon nitride. The region of 3000–3500 cm^{-1} is related to the N−H stretch, whilst the peaks from 1125 to 1875 cm^{-1} are the typical stretching vibration modes of aromatic carbon and nitrogen heterocycles. The sharp peak at 809 cm^{-1} is the out-of-plane bending mode of heptazine rings [17]. It is worth noting the peak at 809 cm^{-1} shifts toward high frequency, and the signal at 1086 cm^{-1} corresponding to the C−O vibration mode becomes stronger with the increase of CH$_3$COONH$_4$ concentration [30]. However, the peak at 980 cm^{-1} corresponding to N−O groups is not found in all samples, proving no N−O species generated in O−CN catalysts [52].

For the sake of uncovering the formation processes of O-CN, TG measurements of precursors (melamine, CH$_3$COONH$_4$ and melamine/CH$_3$COONH$_4$ mixture of 1:10 in molar ratio) have been carried out, as shown in Fig. 3A–C. The thermal polymerization temperature of melamine is about 345 °C and CH$_3$COONH$_4$ completely decomposes at 140 °C. However, a very different TG curve is observed for the melamine/CH$_3$COONH$_4$ mixture, in which two new decomposition temperatures appear at 128 °C and 282 °C. The distinct decomposition temperatures reflect that CH$_3$COONH$_4$ reacts with melamine to form an intermediate at about 128 °C during the thermal-polymerization process, and then the intermediate starts to decompose into O doped g-C$_3$N$_4$ sample with the temperature rising to 282 °C.

The morphology of g-C$_3$N$_4$ and O-CNX (X = 1–3) photocatalyst was observed by SEM and TEM (Fig. S1 and Fig. 4). In comparison with bulk g-C$_3$N$_4$ (Fig. 4A), O substituted g-C$_3$N$_4$ exhibits corroded-like morphology. It is worth mentioning that this microstructure is beneficial to improve the photocatalytic activity by providing more reaction active
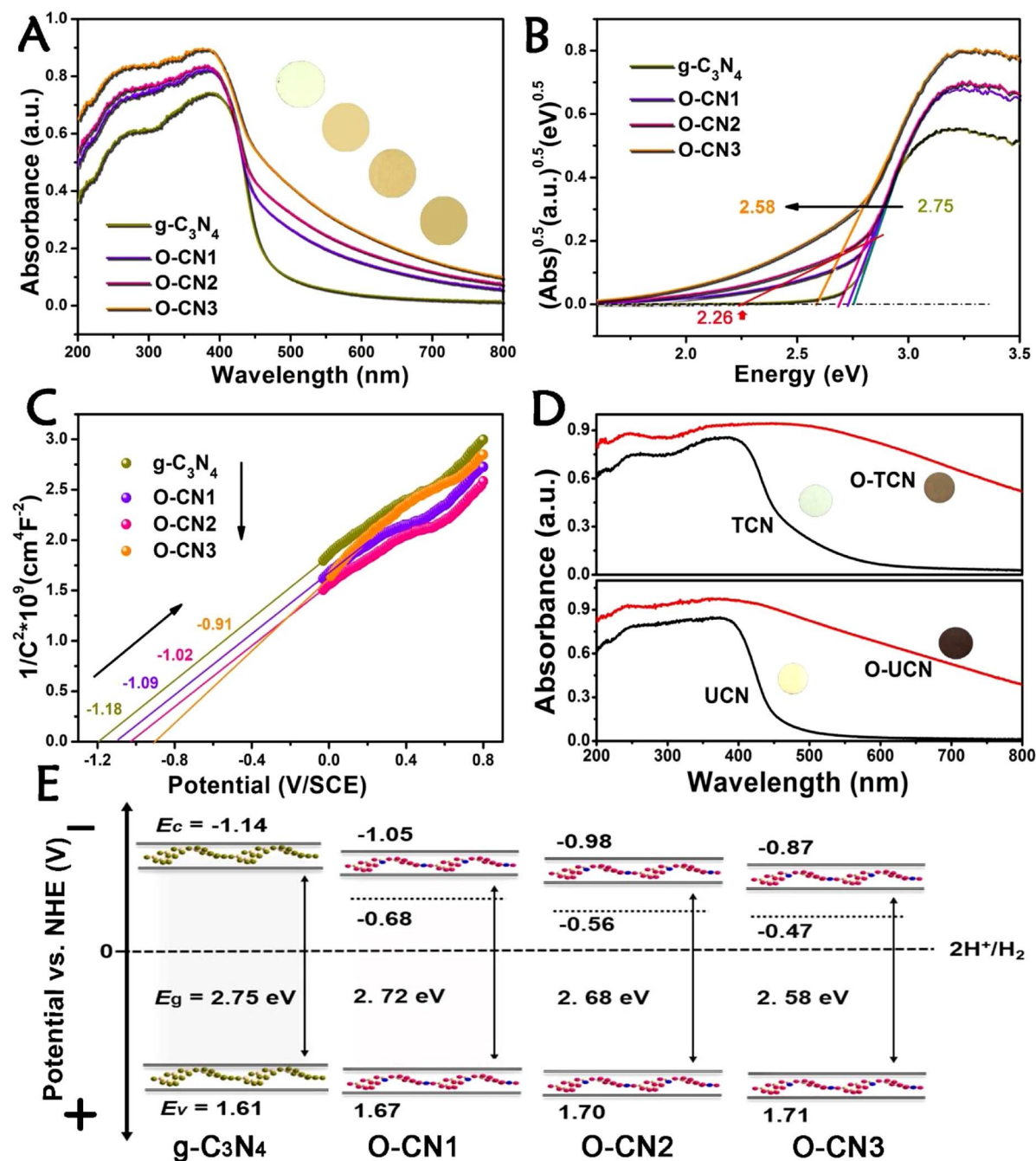
Fig. 5. (A) UV–vis light absorption spectra (insets indicate the corresponding color), (B) Band gaps and (C) Mott-Schottky plots of g-C_3N_4 and O-CNX (X = 1–3) samples. (D) UV–vis light absorption spectra of U(T)CN and O-U(T)CN prepared by urea and thiourea as precursors for replacing melamine (insets show the digital pictures of samples). (E) Band structure alignments for g-C_3N_4 and O-CNX (X = 1–3) samples. (For interpretation of the references to colour in the text, the reader is referred to the web version of this article.)

sites [53]. As shown in Table S1, the BET specific surface areas of O-CNX (X = 1–3) are 20.3, 83.9 and 90.5 m^2/g, respectively, significantly higher than that of bulk g-C_3N_4 (12.1 m^2/g). Fig. 4D–F display the element distribution of carbon (C), nitrogen (N) and oxygen (O), respectively, and all atoms are homogeneously distributed in O substituted g-C_3N_4.

The alterations on optical properties and band structures of O-CNX (X = 1–3) are shown in Fig. 5. It is impressive to note that the light responsive range of g-C_3N_4 is expanded to cover the entire visible-light region owing to O substitution, and the photo-absorption gradually enhances with increasing the CH_3COONH_4 concentration (Fig. 5A). The evidently red-shifted absorption edges from 451 to 481 nm correspond to the bandgap from 2.75 to 2.58 eV calculated by Kubelka-Munk

function (Fig. 5B and Table S1) [54], meeting well with the apparent color change from yellow (g-C_3N_4) to brown (O-CN3) (insets of Fig. 5A). To explain the origin for narrowed bandgap, Mott-Schottky plots of O-CN catalysts were measured. As shown in Fig. 5C, the flat potentials of g-C_3N_4 and O-CNX (X = 1–3) catalysts are calculated to be −1.18, −1.09, −1.02 and −0.91 V versus the Hg/Hg_2Cl_2 electrode, respectively. And they are equivalent to −0.94, −0.85, −0.78 and −0.67 V versus the normal hydrogen electrode (NHE), respectively. Generally, the conduction band (CB) position is 0.1–0.3 eV higher than the flat-band potential for n-type semiconductor [55]. So, the CB positions of g-C_3N_4 and O-CNX (X = 1–3) catalysts can be estimated to be −1.14, −1.05, −0.98 and −0.87 eV, respectively. Based on the bandgaps and CB positions, the valence band (VB) positions of g-C_3N_4
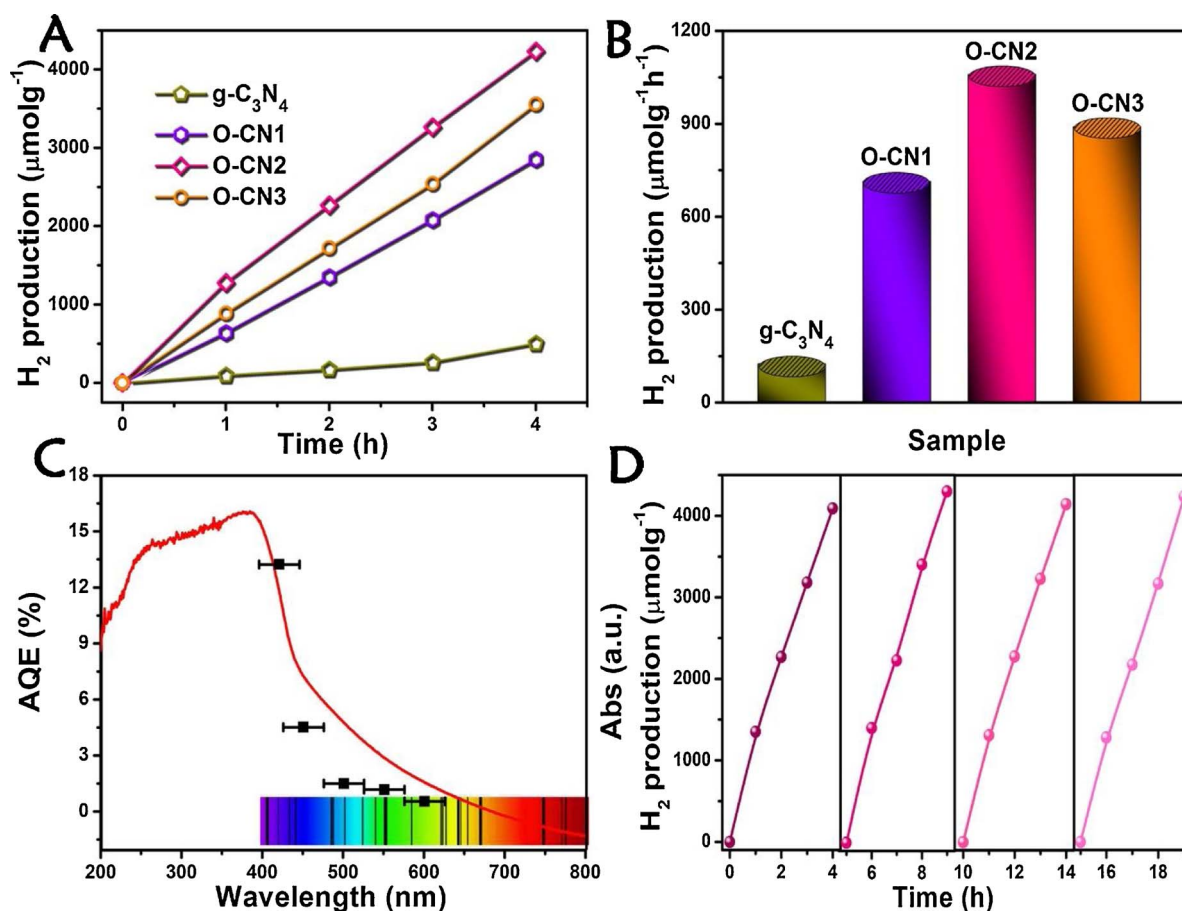
Fig. 6. (A) Photocatalytic H_2 evolution under visible light irradiation ($\lambda > 420\,nm$), and (B) corresponding apparent rate constants of g-C_3N_4 and O-CNX (X = 1–3) samples. (C) UV–vis diffuse-reflectance spectrum and wavelength-dependent AQE of O-CN2. (D) The stability test for four cycling H_2 evolution of O-CN2 under visible light irradiation ($\lambda > 420\,nm$).

and O-CNX (X = 1–3) catalysts are 1.61, 1.67, 1.70 and 1.71 eV, respectively. Interesting, Fig. 5B shows that the bandgaps of O doped g-C_3N_4 present two distinct positive slopes in different potential regions. The second band gaps of O-CN1, O-CN2 and O-CN3 are determined to be 2.35, 2.26 and 2.18 eV, respectively. The value of second band gap could be directly seen as the distance between valence band and acceptor level [56,57]. Therefore, the acceptor levels can be determined as −0.68, −0.56 and −0.47 eV for O-CN1, O-CN2 and O-CN3, respectively. Based on the above results, the band structure diagrams of g-C_3N_4 and O-CNX (X = 1–3) are illustrated in Fig. 5E. The narrowed bandgaps of O substituted g-C_3N_4 are beneficial to absorbing more visible light, and the as-generated acceptor level can easily trap photo-induced electrons and reserve them, reducing the recombination rate of electrons and holes to promote photocatalytic activity. Furthermore, to study the general applicability of the current modification strategy, O substituted g-C_3N_4 samples prepared by other precursors (urea and thiourea) for replacing melamine display similar results that an obviously narrowed bandgap was achieved compared with the pristine g-C_3N_4 (Fig. 5D), showing the universality of this ammonium acetate-assisted O substitution synthetic approach.

The photocatalytic performance of g-C_3N_4 and O-CNX (X = 1–3) samples was evaluated by a typical time course of hydrogen production under visible light irradiation ($\lambda > 420\,nm$) with 1 wt% Pt as co-catalyst at room temperature. As presented in Fig. 6A, all the O substituted g-C_3N_4 samples show largely enhanced H_2 evolution activity, and the O-CN2 sample displays the best photocatalytic performance with the H_2 evolution rate reaching 1062.4 $\mu mol\,h^{-1}\,g^{-1}$, which is approximately 9 times higher than that of bulk g-C_3N_4 (Fig. 6B). The apparent quantum efficiency (AQE) for H_2 evolution of O-CN2 was investigated under various monochromatic light irradiation conditions as shown in Fig. 6C,

which displays the tendency of AQE curve matched well with the UV–vis diffuse reflectance spectrum and a high AQE data of 13.2% under irradiation at 420 nm. The value is higher than the previously reported doped g-C_3N_4 in the literatures (Table S2). Fig. 6D shows the stability test for four cycling H_2 evolution of O-CN2. It reflects that the high photocatalytic H_2 production activity of O-CN2 is well kept at every cycling test, and no phase structure changed after four successive cycles (Fig. S2), verifying the high stability and durability of the catalyst.

To understand the charge transfer among atoms, the charge difference distribution after O substitution in g-C_3N_4 framework is investigated as shown in Fig. 7A and B. The blue sphere represents charge accumulation and yellow sphere represents charge depletion, reflecting that the doped O atom has formed a stable covalent bond with adjacent C atom and the electrons trend to transfer from C atoms to O atoms. In general, electrons in the covalent bond have a tendency to transfer to the atoms with bigger electronegativity. In the O substituted g-C_3N_4, the electronegativity value of O atoms is bigger than that of C atoms. Thus, the electrons transfer from C atoms to O atoms, in accordance with the calculated Δq with Bader method [58], which represents the carried charge of O atom and could be calculated. Therefore, it can be concluded that O substitution could cause the charge redistribution and electron delocalization, resulting in the local charge separation contributing to enhanced photocatalytic activity. The separation efficiency of charge carriers can be reflected by transient photocurrent responses. As shown in Fig. S3, all samples present stable and repeatable transient photocurrent response with on-off cycles under visible light irradiation. Compared to g-C_3N_4, O substituted g-C_3N_4 samples exhibit drastically enhanced photocurrent intensity, demonstrating greatly increased charge transfer efficiency [59–63]. To obtain in-depth insight, the
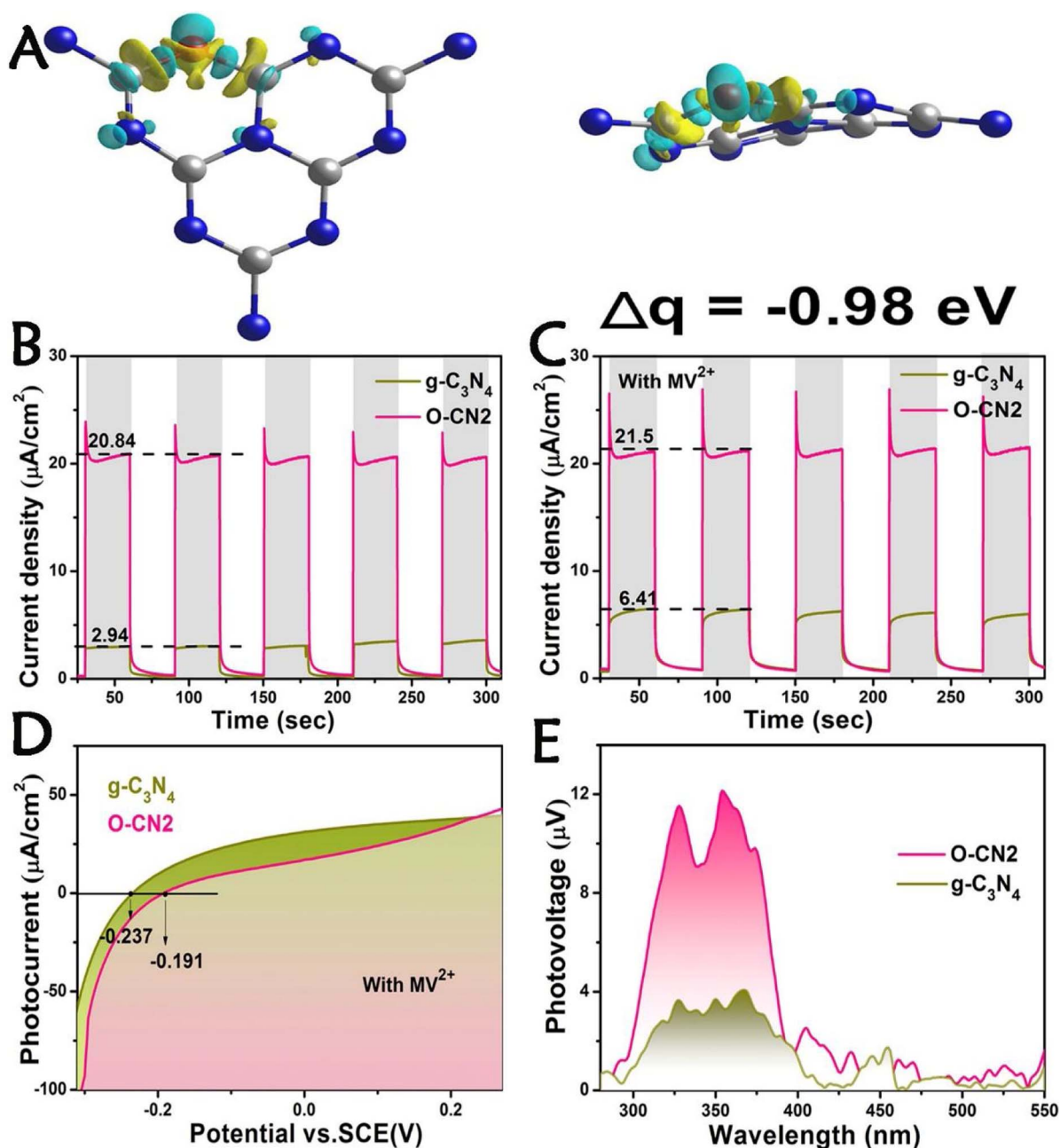
Fig. 7. (A) Charge difference distribution of O substituted g-C$_3$N$_4$ from topview and sideview (the grey and blue atoms stand for C and N atoms, respectively). Δq: negative means electrons adsorption. Transient photocurrent density of g-C$_3$N$_4$ and O-CN2 under visible light (B) without and (C) with adding 0.001M methylviologen dichloride (MVCl$_2$). (D) Linear sweep voltammetry (LSV) with MVCl$_2$ and (E) the surface photovoltage (SPV) spectra of g-C$_3$N$_4$ and O-CN2. (For interpretation of the references to colour in this figure legend, the reader is referred to the web version of this article.)

surface charge transfer efficiency η$_{trans}$ and carrier density of O-CN2 and g-C$_3$N$_4$ were determined. As shown in Fig. 7B and C, the surface charge transfer efficiency η$_{trans}$ is measured by adding a quick electron scavenger (MVCl$_2$) in electrolyte (0.1 M Na$_2$SO$_4$). According to literature, the photocurrent of without MVCl$_2$ can be obtained by the following Eq. (1) [64].

$$J_{H2O} = J_{max}\eta_{abs}\eta_{sep}\eta_{trans} \tag{1}$$

Where J_{H2O} is the measured photocurrent; J_{max} is the theoretical maximum photocurrent; $η_{abs}$ is the light absorption efficiency; $η_{sep}$ is the charge separation efficiency inside the photoanode; $η_{trans}$ is surface charge transfer efficiency of the photoanode.

In the presence of electron scavenger MV^{2+}, the surface charge transfer ($η_{trans}$) is very fast and approximately equals to 100%. So, the

equation of photocurrent can be expressed as Eq(2),

$$J_{MV^{2+}} = J_{max}\eta_{abs}\eta_{sep} \tag{2}$$

As the parameters of J_{max}, $η_{abs}$ and $η_{sep}$ are not changed for both J_{H2O} and $J_{MV^{2+}}$, $η_{trans}$ can be obtained as followed Eq. (3),

$$\eta_{trans} = J_{H2O}/J_{MV^{2+}} \tag{3}$$

When adding electron scavenger MV^{2+} in electrolyte, the photocurrent density of g-C$_3$N$_4$ increases from 2.94 μAcm^{-2} to 6.41 μAcm^{-2}, while that of O-CN2 increases from 20.84 μAcm^{-2} to 21.5 μAcm^{-2}. This increment is attributed to the easier reduction of MV^{2+} than water molecules. The surface charge transfer ($η_{trans}$) of g-C$_3$N$_4$ and O-CN2 is calculated to be 45.8% and 96.6%, respectively. This result suggests the O substitution could efficiently accelerate the charge migration on the

surface of g-C_3N_4, which is beneficial to electron injection into the redox couple in the reaction system. Besides, we also survey the density of charge carriers of catalysts. The photocurrent onset potential in a voltammograms reflects the quasi Fermi level of majority carriers with the existence of MV^{2+} [65]. Since there is hardly any over potential for the reduction of fast electron acceptor MV^{2+}, charge carrier can migrate to the external circuit for photocurrent generation once the applied bias reaches the quasi Fermi level [65]. In Fig. 7D, the potential of O-CN2 (-0.191 V vs. SCE) is 0.046 V positive than that of g-C_3N_4 (-0.237 V vs. SCE). In the quasi Fermi level, the carrier density difference between g-C_3N_4 and O-CN2 can be calculated based on the Nernst Eq. (4) [66,67]

$$E_{f1} - E_{f2} = kT\ln(N_{f1}/N_{f2})/e \tag{4}$$

where E_{f1} and E_{f2} is the quasi Fermi level of sample 1 and 2, respectively; N_{f1} and N_{f2} is the carrier density at the Fermi level of sample 1 and 2, respectively. k is the BoltzmannÏs Constant, T presents the temperature and e is elementary charge. Then, the 0.046 V increment corresponds to 6.3 times higher carrier density of O-CN2, which is greatly helpful for the photocatalytic water splitting. Furthermore, surface photovoltage (SPV) spectra were used to investigate the separation degree of photo-generated charge carriers. Usually, the stronger peak demonstrates a faster separation efficiency of the electron-hole pairs [68,69]. As shown in Fig. 7E, O-CN2 sample shows an obviously stronger SPV response than g-C_3N_4 in the UV–vis light range, which reflects the greatly enhanced charge separation efficiency. The smaller radius of EIS Nyquist plots (Fig. S4) and the increased lifetime (τ) of injected electrons of O-CN2 (Fig. S5) also confirm the efficient charge carriers separation and transfer via O substitution [70–72]. Furthermore, the lower PL emission intensity of O substituted g-C_3N_4 samples suggests the reduced recombination rate of electron-hole pairs (Fig. S6) [73,74]. The above results provide solid evidence that the charge separation and migration efficiency of g-C_3N_4 are remarkably improved owing to O substitution, contributing to the remarkably enhanced photocatalytic performance.

4. Conclusion

In summary, wide-range-photoresponsive O substituted g-C_3N_4 with tunable band structure and efficient charge separation was successfully achieved via introduction of substantial ammonium acetate in the thermal polymerization process of melamine, and the O doping concentration is adjustable from 0.68% to 5.59% by changing the ammonium acetate amount. The experimental characterizations and density functional theory (DFT) calculations disclosed that the replacement of O atoms for lattice N atoms by forming C—O=C bonds for the first time generates an acceptor level, which not only extends the visible light absorption from 450 nm to 800 nm, but also greatly promotes the carrier density, bulk charge separation and surface charge transfer efficiency. Benefiting from these advantages, the O-CN2 sample with O concentration of 2.03% shows the most enhanced hydrogen production activity, which is approximately 9 times higher than that of g-C_3N_4 under visible light irradiation with a high apparent quantum efficiency (AQE) of 13.2% at 420 nm, exceeding most of the reported doped g-C_3N_4. Besides, the similar O substituted g-C_3N_4 samples can also be obtained by pyrolysis of ammonium acetate with other nitrogen-rich precursors (such as urea and thiourea), demonstrating that it is a general approach for O substitution. This work provides a new reference into band structure modulation and charge separation enhancement for developing high-efficiency photocatalyst.

Acknowledgment

Appendix A. Supplementary data

Supplementary material related to this article can be found, in the online version, at doi:https://doi.org/10.1016/j.apcatb.2018.02.038.

References

[1] W.J. Ong, L.L. Tan, Y.H. Ng, S.T. Yong, S.P. Chai, Graphitic carbon nitride (g-C_3N_4)-based photocatalysts for artificial photosynthesis and environmental remediation: are we a step closer to achieving sustainability? Chem. Rev. 116 (2016) 7159–7329.

[2] J. Li, L.J. Cai, J. Shang, Y. Yu, L.Z. Zhang, Giant enhancement of internal electric field boosting bulk charge separation for photocatalysis, Adv. Mater. 28 (2016) 4059–4064.

[3] Y.F. Guo, J. Li, Y.P. Yuan, L. Li, M.Y. Zhang, C.Y. Zhou, Z.Q. Lin, A rapid microwave-assisted thermolysis route to highly crystalline carbon nitrides for efficient hydrogen generation, Angew. Chem. Int. Ed. 55 (2016) 14693–14697.

[4] S. Ye, R. Wang, M.Z. Wu, Y.P. Yuan, A review on g-C_3N_4 for photocatalytic water splitting and CO_2 reduction, Appl. Surf. Sci. 358 (2015) 15–27.

[5] Z. Bian, F. Cao, J. Zhu, H. Li, Plant uptake-assisted round-the-clock photocatalysis for complete purification of aquaculture wastewater using sunlight, Environ. Sci. Technol. 49 (2015) 2418–2424.

[6] Y.P. Yuan, L.S. Yin, S.W. Cao, L.N. Gu, G.S. Xu, P.W. Du, H. Chai, Y.S. Liao, C. Xue, Microwave-assisted heating synthesis: a general and rapid strategy for large-scale production of highly crystalline g-C_3N_4 with enhanced photocatalytic H_2 production, Green Chem. 16 (2014) 4663–4668.

[7] Z. Bian, J. Zhu, H. Li, Solvothermal alcoholysis synthesis of hierarchical TiO_2 with enhanced activity in environmental and energy photocatalysis, J. Photochem. Photobiol. C 28 (2016) 72–86.

[8] H.Y. Li, S.Y. Gan, H.Y. Wang, D.X. Han, L. Niu, Intercorrelated superhybrid of AgBr supported on graphitic-C_3N_4-decorated nitrogen-doped graphene: high engineering photocatalytic activities for water purification and CO_2 reduction, Adv. Mater. 27 (2015) 6906–6913.

[9] G.G. Liu, G.X. Zhao, W. Zhou, Y.Y. Liu, H. Pang, H.B. Zhang, D. Hao, X.G. Meng, P. Li, T. Kako, J.H. Ye, In situ bond modulation of graphitic carbon nitride to construct p-n homojunctions for enhanced photocatalytic hydrogen production, Adv. Funct. Mater. 26 (2016) 6822–6829.

[10] M. Shalom, S. Gimenez, F. Schipper, I. Herraiz-Cardona, J. Bisquert, M. Antonietti, Controlled carbon nitride growth on surfaces for hydrogen evolution electrodes, Angew. Chem. 12 (2014) 3728–3732.

[11] L. Sun, M.J. Yang, J.F. Huang, D.S. Yu, W. Hong, X.D. Chen, Freestanding graphitic carbon nitride photonic crystals for enhanced photocatalysis, Adv. Funct. Mater. 26 (2016) 4943–4950.

[12] Y.X. Li, H. Xu, S.X. Ouyang, D. Lu, X. Wang, D.F. Wang, J.H. Ye, In-situ surface alkalinized g-C3N4 toward enhancement of photocatalytic H_2 evolution under visible-light irradiation, J. Mater. Chem. A 4 (2015) 2943–2950.

[13] C.Y. Liu, H.W. Huang, L.Q. Ye, S.X. Yu, N. Tian, X. Du, T.R. Zhang, Y.H. Zhang, Intermediate-mediated strategy to Horn-like hollow mesoporous ultrathin g-C_3N_4 tube with spatial anisotropic charge separation for superior photocatalytic H_2 evolution, Nano Energy 41 (2017) 738–748.

[14] J. Liu, J.H. Huang, H. Zhou, M. Antoniett, Uniform graphitic carbon nitride nanorod for efficient photocatalytic hydrogen evolution and sustained photoenzymatic catalysis, ACS Appl. Mater. Interfaces 6 (2014) 8434–8440.

[15] S.P. Wang, C.J. Li, T. Wang, P. Zhang, A. Li, J.L. Gong, Controllable synthesis of nanotube-type graphitic C_3N_4 and their visible-light photocatalytic and fluorescent properties, J. Mater. Chem. A 2 (2014) 2885–2890.

[16] Q.J. Fan, J.J. Liu, Y.C. Yu, S.L. Zuo, B.S. Li, A simple fabrication for sulfur doped graphitic carbon nitride porousrods with excellent photocatalytic activity degrading RhB dye, Appl. Surf. Sci. 391 (2016) 360–368.

[17] L.H. Yao, D. Wei, Y.M. Ni, D.P. Yan, C.W. Hu, Surface localization of CdZnS quantum dots onto 2D g-C_3N_4 ultrathin microribbons: highly efficient visible light-induced H_2-generation, Nano Energy 26 (2016) 248–256.

[18] N. Tian, H.W. Huang, Y. He, Y.X. Guo, T.R. Zhang, Y.H. Zhang, Mediator-free direct Z-scheme photocatalytic system: $BiVO_4$/g-C_3N_4 organic-inorganic hybrid photocatalyst with highly efficient visible-light-induced photocatalytic activity, Dalton Trans. 44 (2015) 4297–4307.

[19] Y.F. Li, R.X. Jin, X. Fang, Y. Yang, M. Yang, X.C. Liu, Y. Xing, S.Y. Song, In situ loading of Ag_2WO_4 on ultrathin g-C_3N_4 nanosheets with highlyenhanced photocatalytic performance, J. Hazard. Mater. 313 (2016) 219–228.

[20] D.L. Jiang, J. Li, C.S. Xing, Z.Y. Zhang, S.C. Meng, M. Chen, Two-dimensional CaIn₂S₄/g-C_3N_4 heterojunction nanocomposite with enhanced visible-light photocatalytic activities: interfacial engineering and mechanism insight, ACS. Appl. Mater. Interfaces 7 (2015) 19234.

[21] O. Fontelles-Carceller, M.J. Muñoz-Batista, M. Fernández-García, A. Kubacka, Interface effects in sunlight-driven Ag/g-C_3N_4 composite catalysts: study of the toluene photodegradation quantum efficiency, ACS Appl. Mater. Interfaces 8 (2016) 2617–2627.

[22] J.J. Xue, S.S. Ma, Y.M. Zhou, Z.W. Zhang, M. He, Facile photochemical synthesis of Au/Pt/g-C_3N_4 with plasmon-enhanced photocatalytic activity for antibiotic degradation, ACS Appl. Mater. Interfaces 7 (2015) 9630–9637.

[23] F. Dong, Z.W. Zhao, Y.J. Sun, Y.X. Zhang, S. Yan, Z.B. Wu, An advanced semimetal-organic Bi spheres-g-C_3N_4 nanohybrid with SPR-enhanced visible-light photocatalytic performance for NO purification, Environ. Sci. Technol. 49 (2015) 12432–12440.

[24] N. Tian, Y.H. Zhang, X.W. Li, K. Xiao, X. Du, F. Dong, G.I.N. Waterhouse,

T.R. Zhang, H.W. Huang, Precursor-reforming protocol to 3D mesoporous g-C₃N₄ established by ultrathin self-doped nanosheets for superior hydrogen evolution, Nano Energy 38 (2017) 72–81.

[25] Y.J. Zhang, T. Mori, J.H. Ye, M. Antonietti, Phosphorus-doped carbon nitride solid: enhanced electrical conductivity and photocurrent generation, J. Am. Chem. Soc. 132 (2010) 6294–6295.

[26] G. Liu, P. Niu, C.H. Sun, S.C. Smith, Z.G. Chen, G.Q. Lu, H.M. Cheng, Unique electronic structure induced high photoreactivity of sulfur-doped graphitic C₃N₄, J. Am. Chem. Soc. 132 (2010) 11642–11648.

[27] G.H. Dong, K. Zhao, L.Z. Zhang, Carbon self-doping induced high electronic conductivity and photoreactivity of g-C₃N₄, Chem. Commun. 48 (2012) 6178–6180.

[28] Y. Wang, J.S. Zhang, X.C. Wang, M. Antonietti, H.R. Li, Boron- and fluorine-containing mesoporous carbon nitride polymers: metal-free catalysts for cyclohexane oxidation, Angew. Chem. Int. Ed. 49 (2010) 3356–3359.

[29] S.E. Guo, Y.Q. Tang, Y. Xie, C.G. Tian, Q.M. Feng, W. Zhou, B.J. Jiang, P-doped tubular g-C₃N₄ with surface carbon defects: universal synthesis and enhanced visible-light photocatalytic hydrogen production, Appl. Catal. B: Environ. 218 (2017) 664–671.

[30] X.J. She, J.J. Wu, J. Zhong, H. Xu, Y.C. Yang, R. Vajtai, J. Lou, Y. Liu, D.L. Du, H.M. Li, P.M. Ajayan, Oxygenated monolayer carbon nitride for excellent photocatalytic hydrogen evolution and external quantum efficiency, Nano Energy 27 (2016) 138–146.

[31] Z.F. Huang, J.J. Song, L. Pan, Z.M. Wang, X.Q. Zhang, J.J. Zou, W.B. Mi, X.W. Zhang, L. Wang, Carbon nitride with simultaneous porous network and O-doping for efficient solar-energy-driven hydrogen evolution, Nano Energy 12 (2015) 646–656.

[32] Y.X. Wang, H. Wang, F.Y. Chen, F. Cao, X.H. Zhao, S.G. Meng, Y.J. Cui, Facile synthesis of oxygen doped carbon nitride hollow microsphere for photocatalysis, Appl. Catal. B: Environ. 206 (2017) 417–425.

[33] C.Y. Liu, Y.H. Zhang, F. Dong, X. Du, H.W. Huang, Facilely and synchronously ameliorating charge separation and band energy level in porous g-C₃N₄ for boosting photooxidation and photoreduction ability, J. Phys. Chem. C 120 (2016) 10381–10389.

[34] C.Y. Liu, Y.H. Zhang, F. Dong, A.H. Reshak, L.Q. Ye, N. Pinna, C. Zeng, T.R. Zhang, H.W. Huang, Chlorine intercalation in graphitic carbon nitride for efficient photocatalysis, Appl. Catal. B: Environ. 203 (2017) 465–474.

[35] S. Grimme, Semiempirical GGA-type density functional constructed with a long-range dispersion correction, J. Comput. Chem. 27 (2006) 1787.

[36] G. Kresse, J. Furthmuller, Efficient iterative schemes for ab initio total-energy calculations using a plane-wave basis set, Phys. Rev. B 54 (1996) 11169.

[37] G. Kresse, J. Furthmuller, Efficiency of ab-initio total energy calculations for metals and semiconductors using a plane-wave basis set, Comput. Mater. Sci. 6 (1996) 15.

[38] J.P. Perdew, K. Burke, M. Ernzerhof, Generalized gradient approximation made simple, Phys. Rev. Lett. 77 (1996) 3865.

[39] P.E. Blochl, Projector augmented-wave method, Phys. Rev. B 50 (1994) 17953.

[40] G. Kresse, D. Joubert, From ultrasoft pseudopotentials to the projector augmented-wave method, Phys. Rev. B 59 (1999) 1758.

[41] D.R. Lide, Handbook of Chemistry and Physics, CRC Press, 2003.

[42] J.H. Li, B. Shen, Z.H. Hong, B.Z. Lin, B.F. Gao, Y.L. Chen, A facile approach to synthesize novel oxygen-doped g-C₃N₄ with superior visible-light photoreactivity, Chem. Commun. 48 (2012) 12017–12019.

[43] J.W. Fang, H.Q. Fan, M.M. Li, C.B. Long, Nitrogen self-doped graphitic carbon nitride as efficient visible light photocatalyst for hydrogen evolution, J. Mater. Chem. A 3 (2015) 13819.

[44] S.E. Guo, Z.P. Deng, M.X. Li, B.J. Jiang, C.G. Tian, Q.J. Pan, H.G. Fu, Phosphorus-doped carbon nitride tubes with a layered micronanostructure for enhanced visible-light photocatalytic hydrogen evolution, Angew. Chem. Int. Ed. 55 (2016) 1830–1834.

[45] F. He, G. Chen, Y.G. Yu, S. Hao, Y.S. Zhou, Y. Zheng, Facile approach to synthesize g-PAN/g-C₃N₄ composites with enhanced photocatalytic H₂ evolution activity, ACS Appl. Mater. Interfaces 6 (2014) 7171–7179.

[46] M. Tahir, C.B. Cao, N. Mahmood, F.K. Butt, A. Mahmood, F. Idrees, S. Hussain, M. Tanveer, Z. Ali, I. Aslam, Multifunctional g-C₃N₄ nanofibers: a template-free fabrication and enhanced optical, electrochemical, and photocatalyst properties, ACS Appl. Mater. Interfaces 6 (2014) 1258–1265.

[47] J. Baltrusaitis, P. Jayaweera, V. Grassian, XPS study of nitrogen dioxide adsorption on metal oxide particle surfaces under different environmental conditions, Phys. Chem. Chem. Phys. 11 (2009) 8295–8305.

[48] H.J. Yu, R. Shi, Y.X. Zhao, T. Bian, Y.F. Zhao, C. Zhou, Ge.I.N. Waterhouse, L.Z. Wu, C.H. Tung, T.R. Zhan, Alkali-assisted synthesis of nitrogen deficient graphitic carbon nitride with tunable band structures for efficient visible light-driven hydrogen evolution, Adv. Mater. 16 (2017) 1605148.

[49] H.W. Huang, K. Xiao, N. Tian, F. Dong, T.R. Zhang, X. Du, Y.H. Zhang, Template-free precursor-surface-etching route to porous g-C₃N₄ thin nanosheets for enhancing photocatalytic reduction and oxidation activity, J. Mater. Chem. A 5 (2017) 17452–17463.

[50] Y.P. Yuan, W.T. Xu, L.S. Yin, S.W. Cao, Y.S. Liao, Y.Q. Tng, C. Xue, Large impact of heating time on physical properties and photocatalytic H₂ production of g-C₃N₄ nanosheets synthesized through urea polymerization in Ar atmosphere, Int. J. Hydrogen Energy 38 (2013) 13159–13163.

[51] T. Xiong, W.L. Cen, Y.X. Zhang, F. Dong, Bridging the g-C₃N₄ interlayers for enhanced photocatalysis, ACS Catal. 6 (2016) 2462–2472.

[52] L. Ming, H. Yue, L. Xu, F. Chen, Hydrothermal synthesis of oxidized g-C₃N₄ and its regulation of photocatalytic activity, J. Mater. Chem. A 2 (2014) 19145–19149.

[53] J.S. Zhang, Mi.W. Zhang, C. Yang, X.C. Wang, Nanospherical carbon nitride frameworks with sharp edges accelerating charge collection and separation at a soft photocatalytic interface, Adv. Mater. 26 (2014) 4121–4126.

[54] H.W. Huang, K. Xiao, T.R. Zhang, F. Dong, Y.H. Zhang, Rational design on 3D hierarchical bismuth oxyiodides via in situ self-template phase transformation and phase-junction construction for optimizing photocatalysis against diverse contaminants, Appl. Catal. B: Environ. 203 (2017) 879–888.

[55] H. Kim, P. Borse, W. Choi, J. Lee, Photocatalytic nanodiodes for visible-light photocatalysis, Angew. Chem. Int. Ed. 44 (2005) 4585–4589.

[56] W.H. Feng, Z.B. Fang, B. Wang, L.L. Zhang, Y. Zhang, Y. Yang, M. Huang, S.X. Weng, P. Liu, Grain boundary engineering in organic–inorganic hybrid semiconductor ZnS(en)₀.₅ for visible-light photocatalytic hydrogen production, J. Mater. Chem. A 5 (2017) 1387.

[57] H.W. Huang, X.W. Li, J.J. Wang, F. Dong, P.K. Chu, T.R. Zhang, Y.H. Zhang, Anionic group self-doping as a promising strategy: band-gap engineering and multi-functional applications of high-performance CO_3^{2-}-doped $Bi_2O_2CO_3$, ACS Catal. 5 (2015) 4094–4103.

[58] R. Bader, Atoms in Molecules: A Quantum Theory, Oxford University Press, 1994.

[59] H.W. Huang, X. Han, X.W. Li, S.C. Wang, P.K. Chu, Y.H. Zhang, Fabrication of multiple heterojunctions with tunable visible-light-active photocatalytic reactivity in BiOBr-BiOI full-range composites based on microstructure modulation and band structures, ACS Appl. Mater. Interfaces 7 (2015) 482–492.

[60] A. Zada, M. Humayun, F. Raziq, X.L. Zhang, Y. Qu, L.L. Bai, C.L. Qin, L.Q. Jing, H.G. Fu, Exceptional visible-light-driven cocatalyst-free photocatalytic activity of g-C₃N₄ by well designed nanocomposites with plasmonic Au and SnO₂, Adv. Energy Mater. 6 (2016) 1601190.

[61] H.W. Huang, S.C. Tu, C. Zeng, T.R. Zhang, A.H. Reshak, Y.H. Zhang, Macroscopic polarization enhancement promoting photo- and piezoelectric-induced charge separation and molecular oxygen activation, Angew. Chem. Int. Ed. 56 (2017) 11860–11864.

[62] H.W. Huang, Y. He, X.W. Li, M. Li, C. Zeng, F. Dong, X. Du, T.R. Zhang, Y.H. Zhang, Non-centrosymmetric $Bi_2O_2(OH)(NO3)$ as a desirable $[Bi_2O_2]^{2+}$ layered photocatalyst: strong intrinsic polarity, rational band structure and {001} active exposing facets co-benefiting for robust photooxidating capability, J. Mater. Chem. A 3 (2015) 24547–24556.

[63] H.W. Huang, R.R. Cao, S.X. Yu, K. Xu, W.C. Hao, Y.G. Wang, F. Dong, T.R. Zhang, Y.H. Zhang, Single-unit-cell layer established Bi₂WO₆ 3D hierarchical architectures: efficient adsorption, photocatalysis and dye-sensitized photoelectrochemical performance, Appl. Catal. B: Environ. 219 (2017) 526–537.

[64] G. Liu, J. Shi, F. Zhang, Z. Chen, J. Han, C. Ding, S. Chen, Z. Wang, H. Han, C. Li, A tantalum nitride photoanode modified with a hole-storage layer for highly stable solar water splitting, Angew. Chem. Int. Ed. 53 (2014) 7295–7299.

[65] J. Zhao, M.A. Holmes, F.E. Osterloh, Quantum confinement controls photocatalysis: a free energy analysis for photocatalytic proton reduction at CdSe nanocrystals, ACS Nano 7 (2013) 4316–4325.

[66] B.A. Nail, J.M. Fields, J. Zhao, J. Wang, M.J. Greaney, R.L. Brutchey, F.E. Osterloh, Nickel oxide particles catalyze photochemical hydrogen evolution from water-nanoscaling promotes P-type character and minority carrier extraction, ACS Nano 9 (2015) 5135–5142.

[67] J.C. Hill, A.T. Landers, J.A. Switzer, An electrodeposited inhomogeneous metal-insulator-semiconductor junction for efficient photoelectrochemical water oxidation, Nat. Mater. 14 (2015) 1150–1155.

[68] P. Wang, T.F. Xie, H.Y. Li, L. Peng, Y. Zhang, T.S. Wu, S. Pang, Y.F. Zhao, D.J. Wang, Synthesis and plasmon-induced charge-transfer properties of monodisperse gold-doped titania microspheres, Chem.-Eur. J. 15 (2009) 4366.

[69] L. Peng, T. Xie, Y. Lu, H. Fan, D. Wang, Synthesis, photoelectric properties and photocatalytic activity of the Fe₂O₃/TiO₂ heterogeneous photocatalysts, Phys. Chem. Chem. Phys. 12 (2010) 8033–8041.

[70] X.Q. Fan, L.X. Zhang, R.L. Cheng, M. Wang, M.L. Li, Y.J. Zhou, J.L. Shi, Construction of graphitic C₃N₄-based intramolecular donor-acceptor conjugated copolymers for photocatalytic hydrogen evolution, ACS Catal. 5 (2015) 5008–5015.

[71] Y.X. Guo, H.W. Huang, Y. He, N. Tian, T.R. Zhang, P.K. Chu, Q. An, Y.H. Zhang, In situ crystallization for fabrication of a core–satellite structured BiOBr-CdS heterostructure with excellent visible-light responsive photoreactivity, Nanoscale 7 (2015) 11702.

[72] Z.A. Lan, G.G. Zhang, X.C. Wang, A facile synthesis of Br-modified g-C₃N₄ semiconductors for photoredox water splitting, Appl. Catal. B: Environ. 192 (2016) 116–125.

[73] H.W. Huang, Y. He, X. Du, P.K. Chu, Y.H. Zhang, A general and facile approach to heterostructured core/shell BiVO₄/BiOI p-n junction: room-temperature in situ assembly and highly boosted visible-light photocatalysis, ACS Sustainable Chem. Eng. 3 (2015) 3262–3270.

[74] L. Lin, P. Ye, C. Cao, Q. Jin, G.S. Xu, Y.H. Shen, Y.P. Yuan, Rapid microwave-assisted green production of a crystalline polyimide for enhanced visible-light-induced photocatalytic hydrogen production, J. Mater. Chem. A 3 (2015) 10205–10208.